Received: 20 July 2023 | Revised: 26 October 2023 | Accepted: 20 December 2023

DOI: 10.1002/mawe.202300233

ARTICLE

WILEY VCH

Improved photocatalytic performance via air-plasma modification of titanium dioxide: Insights from experiments and simulations

Verbessertes photokatalytisches Verhalten durch Luft-Plasma-Modifizierung von Titandioxid: Erkenntnisse aus Versuchen und Simulationen

C. Ugwumadu[1] | **O. Ibukun**[2, 3] | **H. K. Jeong**[4] | **D. A. Drabold**[1]

[1]Department of Physics and Astronomy, Nanoscale and Quantum Phenomena Institute (NQPI), Ohio University, Athens, USA

[2]Department of Physical Chemistry, Freie Universität Berlin, Berlin, Germany

[3]Helmholtz-Zentrum, Berlin, Germany

[4]Department of Materials-Energy Science and Engineering, Institute of Industry and Technique Daegu University, Gyeongsan Republic of Korea

Correspondence
C. Ugwumadu, Department of Physics and Astronomy, Nanoscale and Quantum Phenomena Institute (NQPI), Ohio University, Athens, Ohio 45701, USA.
Email: cu884120@ohio.edu

Funding information
Nanoscale & Quantum Phenomena Institute (NQPI); National Science Foundation (NSF), Grant/Award Number: ACI-1548562, DMR-190008P; ACCESS, Grant/Award Number: 2138259, 2138286, 2138307, 2137603, 2138296, phy230007p; National Research Foundation of Korea, Grant/Award Number: NRF-2020R1I1A3A04037469

Abstract

Commercial titanium dioxide is successfully plasma-treated under ambient conditions for different periods, leading to reduced crystallite size and the creation of oxygen vacancies. Density functional theory-based calculations reveal the emergence of additional localized states close to the conduction band, primarily associated with under-coordinated titanium atoms in non-stoichiometric titanium-oxide systems. The plasma-treated samples exhibit improved photocatalytic performance in the degradation of methylene blue compared to untreated samples. Moreover, the 4-hour plasma-treated photocatalyst demonstrates commendable stability and reusability. This work highlights the potential of cost-effective plasma treatment as a simple modification technique to significantly enhance the photocatalytic capabilities of titanium-oxide materials.

KEYWORDS
molecular simulation, photocatalysis, plasma treatment, titanium dioxide, ultraviolet light

SCHLÜSSELWÖRTER
Fotokatalyse, molekulare Simulation, Plasmabehandlung, Titandioxid, ultraviolettes Licht

1 | INTRODUCTION

Industrial activities, such as leather, paper, and textile production, generate hazardous waste containing the cationic dye, methylene blue (MB), which poses significant health risks and requires effective removal from industrial effluents [1, 2]. Titanium dioxide (TiO_2) and its composites have emerged as highly versatile compounds with applications in hydrogen evolution reactions and sensor devices, but their most crucial application is as photocatalysts [3–5]. Materials comprising titanium oxide in various forms have displayed substantial potential as highly efficient photocatalysts for a wide range of reactions involved in water and air purification [6–9]. This efficacy is primarily attributed to their chemical stability, non-toxic nature, and exceptional reactivity.

Titanium oxide-based photocatalysts operate by generating electron-hole pairs through band gap excitation. These pairs are subsequently transferred to surface-adsorbed substrates, a process influenced by the competition of charge recombination. Thus, the efficiency of titanium oxide as a photocatalyst largely depends on its ability to efficiently separate charges, its surface area, and the exposure of reactive facets to the environment. However, commercial titanium dioxide possesses low surface area, a wide bandgap, and rapid charge recombination, all limiting its photocatalytic efficiency.

Several strategies have been devised to enhance the photocatalytic performance of titanium oxide materials. These methods include nonmetal or metal doping, synthesis of "black" titanium dioxide, expansion of surface area through chemical treatments and sol-gel synthesis, deposition on high-surface-area substrates like graphene, and the use of hydrothermal methods [10–16]. These modifications commonly alter the band structure of titanium oxide, extending its absorption range and/or improving charge separation, thus reducing electron-hole pair recombination time.

Another cost-effective method to enhance the photocatalytic performance of titanium dioxide is through plasma treatment. This modification technique increases the effective surface area, improves hydrophilicity, and enhances reactivity by creating highly reactive species like oxygen radicals and vacancies, which in turn leads to the formation of defective species like Ti^{3+} [17–20]. The active sites facilitate the breakdown of organic pollutants and other molecules during photocatalysis via a delayed electron-hole recombination process. This study explores the improved photocatalytic activity of plasma-modified titanium dioxide under ambient conditions. To investigate the influence of treatment time, samples treated from one to four hours were analyzed. The investigations include changes in its morphology, chemical speciation, and charge-transfer resistance, along with evaluating the composites' photocatalytic performance in methylene blue degradation.

Molecular dynamics simulations have emerged as an indispensable tool to provide insights into the atomistic characteristics of titanium-oxide materials that hold paramount importance in predicting their photocatalytic performance. Many investigations have aimed to reveal crucial material properties using molecular dynamics simulation, including structural features (bond dimensions, angles, and dihedrals), energetic factors (total/activation energies, heats of formation, and thermodynamic properties), spectroscopic characteristics (vibrational patterns, chemical shifts, and absorption onsets), and electronic attributes (band structures, density of states, and charge redistribution) [21–25].

Preceding any molecular simulation investigation of titanium-oxide systems, the foremost priority is the construction of precise computer models that faithfully represent the material of interest. The quality of the calculations heavily relies on establishing an appropriate starting geometry [26–29]. To illustrate, attempting to characterize the properties of a non-stoichiometric, amorphous variant of a modified titanium-oxide material by employing a crystalline structure of stoichiometric titanium dioxide can lead to erroneous conclusions. Hence, attention must be devoted to this critical phase of the research. In this context, and to provide support to experimental observations, this study also employs density functional theory within the Vienna ab initio simulation package (VASP) to particularly examine the impact of oxygen vacancies on the electronic density of states of titanium suboxides (TiO_{2-x}, where $x < 2$). The discussion is limited to the creation of localized electronic states in the gap region between the valence band minimum and conduction band maximum. The computer models are constructed using a well-defined protocol that begins with randomly distributed titanium and oxygen atoms in a cubic box. This procedure leads from stoichiometric to non-stoichiometric titanium-oxide models, ultimately resulting in representative structures of the amorphous phase induced by plasma treatment of crystalline titanium dioxide.

Overall, the results obtained from this work highlight the potential of air-plasma treatment as a cost-effective and promising approach to tailor titanium dioxide properties for efficient industrial dye degradation and environmental remediation.

2 | MATERIALS AND METHODS

2.1 | Sample preparation

50 mg of titanium dioxide (99.8%, CAS No: 1317–70-0, Sigma-Aldrich) was uniformly spread in a flat-bottom tube (35 mm ×12 mm soda lime glass) and wetted with 200 μL of deionized water to ensure surface uniformity. The plasma treatment was conducted at atmospheric pressure using a discharge potential of 15 kV and a frequency of 25 kHz. The anode material was a stainless-steel needle that was positioned 20 mm apart from a copper tape cathode as described elsewhere [30–33]. The prepared samples were divided into five groups based on the duration of plasma treatment (ranging from 0 h to 4 h). The underlying mechanisms at play during plasma treatment of titanium dioxide involve the energetic bombardment of its surface by highly reactive plasma species. The high temperatures and kinetic energies associated with plasma treatment provide oxygen atoms with the necessary thermal energy to escape their binding sites within the crystal lattice, leading to oxygen vacancy formation. However, as the concentration of oxygen vacancies in titanium dioxide increases the number of available vacant lattice sites decreases [34, 35]. Consequently, introducing additional vacancies becomes progressively more challenging. It is worth mentioning that, while this work does not provide explicit details, the initial analysis involved plasma treatment for a 5-hour duration. Nevertheless, there were no discernible improvements compared to the 4-hour treatment, leading to the discontinuation of the evaluation of the 5-hour plasma-treated samples. This observation reflects the delicate equilibrium between the energy input from plasma treatment and the intrinsic constraints imposed by the crystal lattice's ability to accommodate oxygen vacancies in titanium-oxide systems.

To minimize statistical error, three samples were prepared in each group for subsequent experiments, resulting in a total of 15 samples. The plasma-treated samples were labeled as Pξh (where $\xi = 1, 2, 3, 4$), while three precursors (untreated samples) served as controls and were labeled as P0h. After plasma treatment, the samples were washed and filtered using deionized water followed by drying in a vacuum oven at 60 °C for 24 hours. Methylene blue dye, purchased from Sigma-Aldrich, was used without any treatment to assess the photocatalytic degradation capability of the samples.

2.2 | Structural, physiochemical, and electrochemical analysis

The surface morphology and elemental analysis were examined using a field emission scanning electron microscope with an integrated energy-dispersive x-ray spectrometer. The structure and crystallite size of the prepared samples were analyzed using an x-ray diffractometer with a copper K_α radiation source. The chemical configuration was investigated using x-ray photoelectron spectroscopy with an aluminum K_α x-ray source, and a pass energy of 20 eV.

Photo-electrochemical characterizations were performed using a three-electrode system with one mole of sulfuric acid used as the electrolyte. The Bio-logic (SP-150) EC-Lab instrument was used for electrochemical performance investigations. The working electrode was a glassy carbon electrode, with silver/silver-chloride as the reference electrode and platinum wire as the counter electrode. For analysis, a dispersion of the sample in isopropyl alcohol was drop-casted on the working electrode. Additionally, Electrochemical impedance spectroscopy was conducted in the frequency range of 100 MHz to 500 kHz for photo-electrochemical characterization.

The photodegradation experiments were conducted at room temperature using methylene blue solution with a concentration of 1.6×10^{-4} M (10 mg in 200 mL of deionized water). 40 mg of the samples were added to this solution in a 35 mm ×12 mm flat bottom glass tube. The mixture was magnetically stirred in the dark for 30 minutes to establish absorption/desorption equilibrium. At specific time intervals during the irradiation, 3 mL of the solution was extracted and centrifuged at 7000 min^{-1} for 30 minutes to remove any remaining photocatalyst. The dye content in the centrifuged solution was analyzed using an ultraviolet-visible spectroscopy spectrometer. Additionally, the photocurrent responses of the samples were measured at a constant potential of +1.0 V with on-off intervals of ultraviolet irradiation lasting 30 seconds.

2.3 | Molecular simulation

Three models of stoichiometric titanium dioxide (TiO_2) were generated using the quench-from-melt scheme, which has been successfully utilized in building models of titanium-oxides [26, 27, 36]. Using this approach, 192 atoms, consisting of 64 and 128 titanium and oxygen

atoms respectively, were randomly distributed in a cubic box to achieve a density of 3.8 g/cm^3. To simulate melt, the models were annealed at 2500 K for 9 ps, After the first 2 ps, 3 liquid titanium dioxide configurations were selected at 2 ps intervals till the end of the annealing simulation. Each model was then independently cooled to 2200 K over 5 ps and equilibrated for another 5 ps. The models were further cooled to 1200 K at a rate of 80 K/ps and then equilibrated at this temperature for 2 ps. After this, they were taken to 300 K at a rate of 75 K/ps followed by conjugate gradient relaxation to an energy-minimum configuration.

To simulate oxygen-vacancies in non-stoichiometric titanium suboxide, depicted as TiO_{2-x} (where $x<2$), the models were initiated by randomly removing oxygen atoms from the stoichiometric structures. Following this, the systems underwent a two-step process: first, they were heated to 550 K over 2 ps, then gradually cooled down to 300 K within 2.5 ps. Subsequently, the models were subjected to relaxation until they reached an energy-minimized configuration using conjugate gradient relaxation. Given that the distribution of vacancies significantly impacts electronic localization and stability, a set of nine models was constructed. These models consisted of three variations, each containing 1, 5, or 10 oxygen vacancies. The ensuing discussion in this work encompasses observations made across all these models.

The calculations were implemented within the Vienna *ab initio* simulation package (VASP). The models were constructed using the Perdew-Burke-Ernzerhof (PBE) generalized gradient approximation (GGA) for the exchange-correlation functional [37]. A plane-wave basis set with a kinetic energy of 450 eV was used to expand the electronic wave functions. Since generalized-gradient approximation does not provide the correct electronic structure of the oxides of titanium, the electronic structure calculations were performed using the generalized gradient approximation with the Hubbard U correction, which is generally accepted to improve the electronic structure results [22,23]. Values for U, between 2 eV to 3 eV, been reported to correctly describe the excess electrons localization on titanium sites (Ti 3d states), hence in this work, a U value of 2.5 eV was utilized [22,23]. Static calculations were performed using a plane-wave cutoff of 540 eV with a convergence criterion of 10^{-5} eV. All simulations were performed under periodic boundary conditions using a single Γ k-point.

3 | RESULTS AND DISCUSSION

Hydrophilicity plays a crucial role in aiding photocatalysis, particularly in the context of photocatalytic reactions driven by semiconductor materials such as titanium dioxide or other similar photocatalysts. A physical examination of the hydrophilicity of the samples was conducted by mixing the samples with distilled water to create suspension and then allowing this mixture to settle on a flat surface. The untreated P0h sample settled after just 1 hour, whereas the P4h sample took up to 4 hours to fully settle. The inclusion of a 5-hour treated sample demonstrates that plasma treatment duration of 4 hours yields optimal hydrophilicity, Figure 1. These results indicate that plasma treatment enhanced the hydrophilicity of the titanium-dioxide, resulting in a stronger affinity for water molecules. Consequently, providing

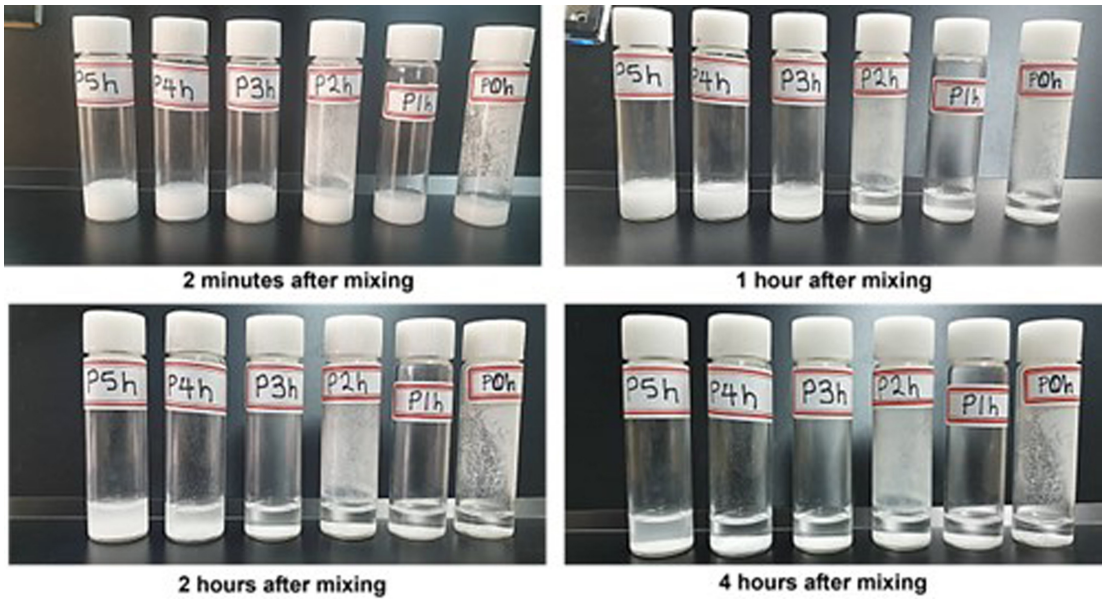

FIGURE 1 Visual inspection of the samples' hydrophilic characteristics over time.

more reactive sites for photocatalytic reactions and facilitating the generation of highly reactive hydroxyl radicals (•OH) – crucial for pollutant degradation. Moreover, hydrophilicity of the photocatalyst surface minimizes aggregation or agglomeration, which can impede photocatalytic activity.

The x-ray diffraction peaks for the untreated sample (P0h) were observed at 25.1°, 36.7°, 37.6°, 38.3°, 47.9°, 53.7°, 54.9°, and 61.9°. These peaks align close to the (101), (103), (004), (112), (200), (105), (211), and (204) crystallographic planes of anatase titanium dioxide (JCPDS no. 00–021-1272), Figure 2. While the plasma-treated samples exhibited similar diffraction peaks, their intensities decreased with increasing treatment duration. Notably, for P4h, the (103) and (112) peaks nearly disappeared. Additionally, the prominent peak at 25.1° slightly shifted to 25.08°, 24.72°, 24.56°, and 24.58° in P1h, P2h, P3 h, and P4h, respectively. These shifts and intensity reductions in the diffraction peaks could have resulted from several factors, including structural modifications, lattice defects, or the presence of impurities due to the plasma process.

To investigate the underlying cause of the reduced peak intensity, we utilized the modified Scherrer formula to obtain the average crystallite size of the samples

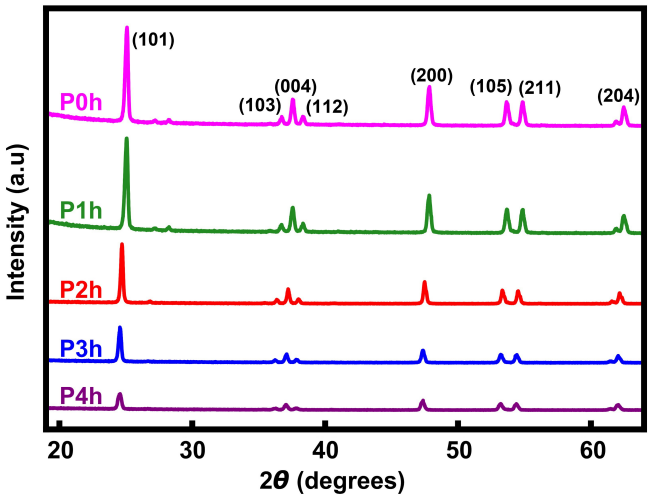

FIGURE 2 X-ray diffraction spectrum for the samples. The spectra were shifted vertically for clarity.

based on the width of the x-ray diffraction peaks [38]. We start by taking the logarithm of the basic Scherrer formula [39]:

$$ln\beta = ln\frac{K \cdot \lambda}{D} + ln\frac{1}{cos(\theta)} \quad (1)$$

where D is the average crystallite size, K is the shape factor (typically taken as 0.9), λ is the x-ray wavelength, β is the full width at half-maximum (FWHM) of the diffraction peaks for 2θ values corresponding to the (101), (105) and (204) planes. The single-valued crystallite size (D), which decreased with increasing plasma treatment duration, was obtained from the exponent of the intercept $\left(e^{ln\frac{K\cdot\lambda}{D}}\right)$ in the linear plot of $ln\beta$ vs $ln(1/cos\theta)$, second column in Table 1. Additionally, scanning electron microscope images of the sample's surface morphology indicates that the samples exhibited a finer structure as the plasma treatment time increased, Figure 3. Particularly, P4h displayed a smooth and refined texture compared to the rough structure of P0h – a consequence of the reduced crystallite size.

The elemental composition of the samples from the energy dispersive spectroscopy measurements indicates that the plasma treatment significantly reduced the relative atomic weight percentage of oxygen in the treated samples, Table 1 (third and fourth columns). This reduction in oxygen content prompted further investigations into the chemical state of the samples, carried out using x-ray photoelectron spectroscopy measurements. The

TABLE 1 Average crystallite sizes (D) calculated using Scherrer formula (column II), and the relative weight percentages of titanium and oxygen in the samples, obtained from the energy dispersive spectroscopy analysis (columns III and IV).

Sample	D [nm]	Ti [wt. %]	O [wt. %]
0 h	35.91	61.41	38.59
P1h	34.42	62.70	37.29
P2h	30.44	65.14	34.86
P3 h	29.18	65.73	34.37
P4h	26.13	67.99	32.01

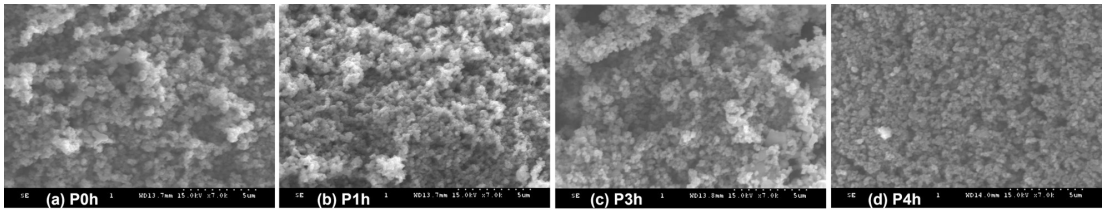

FIGURE 3 Scanning electron microscope images for the samples; (a) P0h, (b) P1h, (c) P3 h, and (d) P4h.

results revealed a remarkable shift in the peaks corresponding to titanium-2p states, Figure 4. In the pristine sample (P0h), distinct titanium 2p doublet peaks were observed at 459.1 eV and 464.8 eV, representing the $Ti^{4+}2p_{3/2}$ and $Ti^{4+}2p_{1/2}$ states, respectively. However, in P4h, these doublet states were shifted to higher energies, specifically at 459.5 eV and 465.4 eV, respectively. Interestingly, a deconvolution analysis of the P4h spectrum revealed the presence of an additional state at 460.1 eV, corresponding to the $Ti^{3+}2p_{3/2}$ state. The observed shift in energy and the emergence of the Ti^{3+} state in the plasma-treated sample result from oxygen vacancies within the system. These vacancies, in turn, give rise to donor states located within the bandgap of titanium dioxide [40].

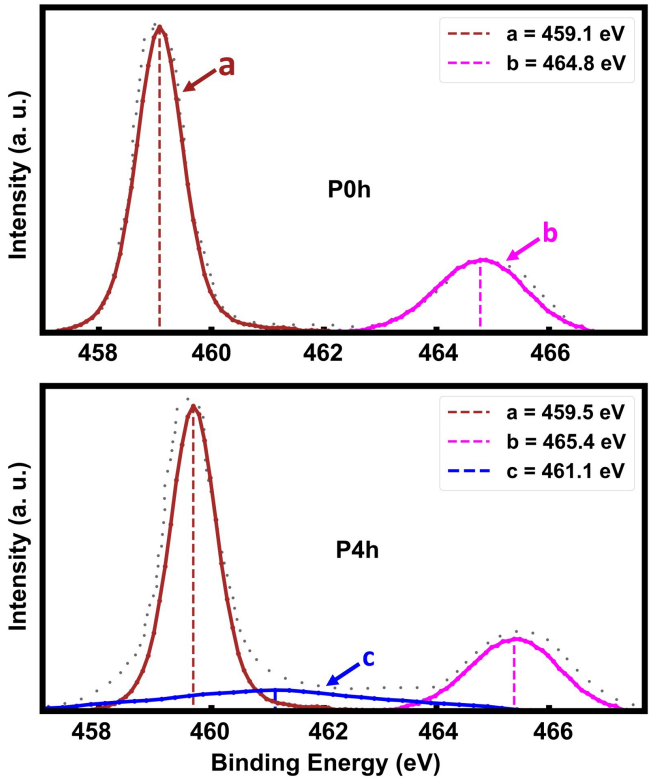

FIGURE 4 X-ray photoelectron spectroscopy data showing the (a) Ti4+2p3/2, (b) Ti4+2p1/2, and (c) Ti3+2p3/2 states of P0h and P4h samples.

Molecular dynamics simulations were employed to complement the x-ray photoelectron spectroscopy measurements, offering additional insight into the manifestation of Ti^{3+} species due to the presence of oxygen vacancy sites. Within these simulations, the electronic structure of stoichiometric titanium dioxide (TiO_2) showed a clear gap region situated between the valence band minimum and conduction band maximum, Figure 5a. Notably, the width of the band-gap in stoichiometric titanium dioxide approximates 2.3 eV, consistent with previous findings for the anatase phase of titanium dioxide [41,42].

In contrast, the introduction of oxygen vacancies into the models, forming non-stoichiometric titanium-oxide (TiO_{2-x}), resulted in the emergence of new Kohn-Sham states within the gap region, Figure 5b–d. The presence of these gap states introduces additional energy levels which serve as effective traps for photogenerated electrons, significantly impeding rapid electron-hole recombination [43]. This trap states promote efficient charge carrier separation by enabling photo-generated electrons to actively engage in redox reactions on the surface of titanium-oxide-based photocatalyst.

Unlike the models featuring 1 and 10 oxygen vacancy sites, the electronic density of states for the model with 5

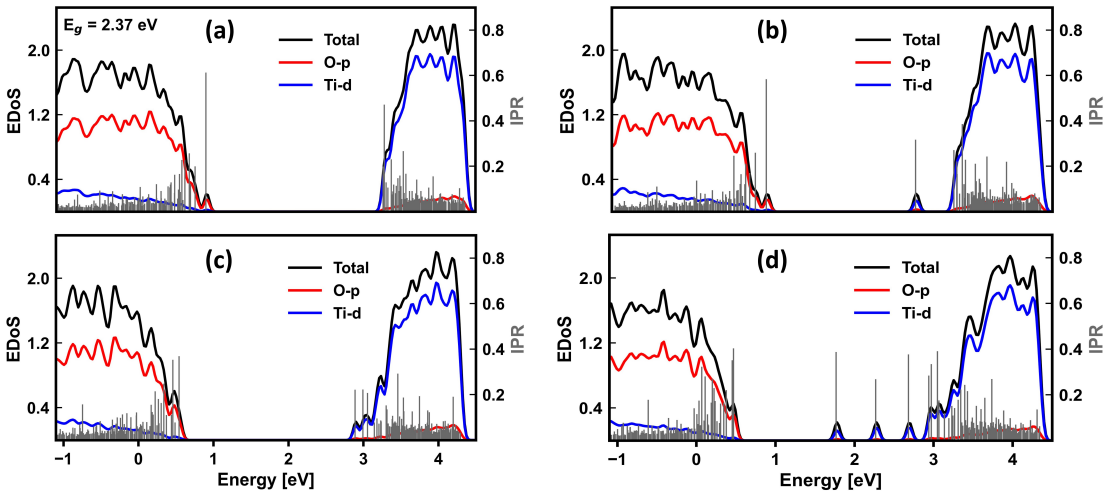

FIGURE 5 Total (black line) and partial (colored lines) electronic density of states (EDoS) plots for stoichiometric (a) and non-stoichiometric titanium-oxides with 1, 5, and 10 oxygen vacancy sites (b, c, and d respectively). The gray lines represent the extent of localization of the Kohn-Sham states, as calculated using the inverse participation ratio (IPR).

oxygen vacancy sites did not exhibit localized states within the gap, Figure 5c. While the complex interplay between vacancy distribution, electron localization, and structural stability is beyond the scope of this work, an in-depth analysis is anticipated in future research. Nevertheless, it is worth appreciating the intricacy of this relationship by comparing the energy-optimized local conformation of the model featuring 5 oxygen vacancy sites before and after vacancy creation. During the energy minimization phase, a substantial number of under-coordinated titanium atoms, resulting from the oxygen vacancies, exhibited a strong preference for forming new bonds with 2-coordinated oxygen atoms in their vicinity, effectively stabilizing back to their initial bond coordination before the oxygen vacancies arose, Figure 6. This bond rearrangement did not occur in all the models, an example is the model with a single oxygen vacancy site where the titanium atoms did not form new bonds after relaxation, Figure 7.

The extent of localization of the Kohn-Sham states (ϕ) was quantified using the electronic inverse participation ratio (IPR) as defined by Equation 2 [44,45]:

$$I(\phi_n) = \frac{\sum_i |a_n^i|^4}{\left(\sum_i |a_n^i|^2\right)^2} \quad (2)$$

where a_n^i denotes the contribution to the eigenvector (ϕ_n) from the i^{th} atomic orbital. The IPR with high (low) values indicates localized (extended) states, gray lines in Figure 5. The states created in the gap region were localized on the titanium atoms, blue line in Figure 5b, d. This phenomenon was particularly evident in the model with a single oxygen vacancy, where the dangling bonds on the titanium atoms, a consequence of the oxygen vacancies, remained immobile. These under-coordinated titanium atoms did not establish bonds with any other oxygen atoms in their relaxed configuration. Consequently, the defective state resulted in the presence of a localized state, at 2.76 eV. The projection of the localized states on the atoms indicated that the state was exclusively localized on the 3 titanium atoms that were initially bonded to the removed oxygen atom that created the vacancy site, Figure 7.

Although no clear gap state was observed for the titanium-oxide model with 5 oxygen vacancy sites, there were notable manifestations of states with appreciable inverse participation ratio values occurring at the tails of

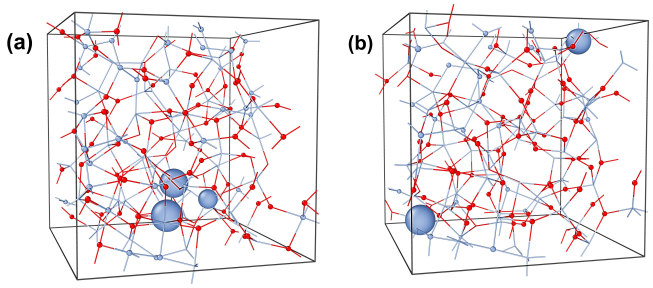

FIGURE 7 The projection of the localized state at 2.76 eV in the model with 1 oxygen vacancy (discussed in Figure 5b). In (a), the black oxygen atom marks the vacancy's location, and the predominantly responsible titanium atoms are depicted in blue. Atom contributions to the localized state are indicated by their size, with larger radii indicating greater localization. Oxygen and titanium atoms are shown in gray and red, respectively.

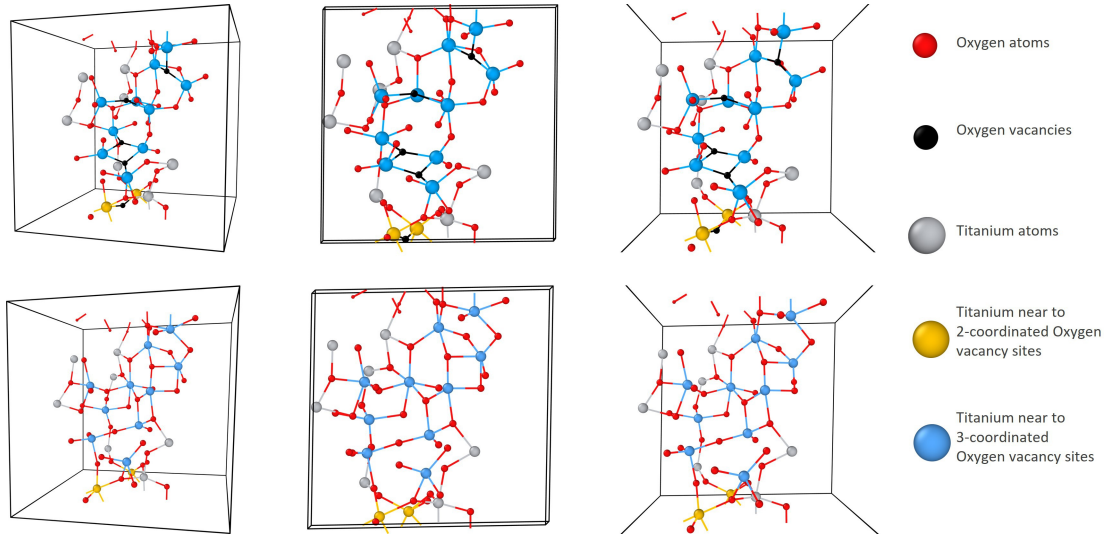

FIGURE 6 The upper panel shows the stoichiometric titanium dioxide model before random oxygen vacancy creation (the oxygen atoms that create the vacancies are shown in black). The lower panel displays the energy-optimized configuration. Titanium atoms near the oxygen vacancy are color-coded: yellow (2-coordinated oxygen proximity) and blue (3-coordinated oxygen proximity). Red and gray colors represent other oxygen and titanium atoms, respectively.

the conduction band, Figure 5c. Nevertheless, a closer examination of the projection of these states onto the atoms in the energy range from 2.84 eV to 3.09 eV, indicates that they were not truly localized, as they were distributed across a limited number of atoms, Figure 8. This „pseudo-localization" phenomenon can be attributed to the stabilization of the under-coordinated titanium atoms following energy relaxation, leading to a system-wide restructuring. The restructuring resulted in strained bonds in specific regions of the model to compensate for the structural rearrangement. These observations portray the influence of vacancy distribution on electron localization and the stability of these defective structures, a facet further complicated by the local amorphous structure of the non-stoichiometric titanium-oxide system.

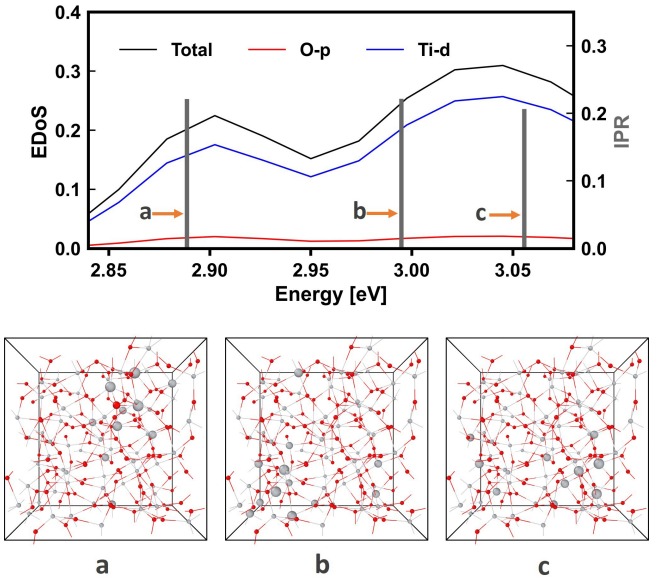

FIGURE 8 Localized states near the conduction band edge in a non-stoichiometric titanium-oxide with five oxygen vacancy sites. These states (a, b, and c) are projected on the atoms in the lower panel.

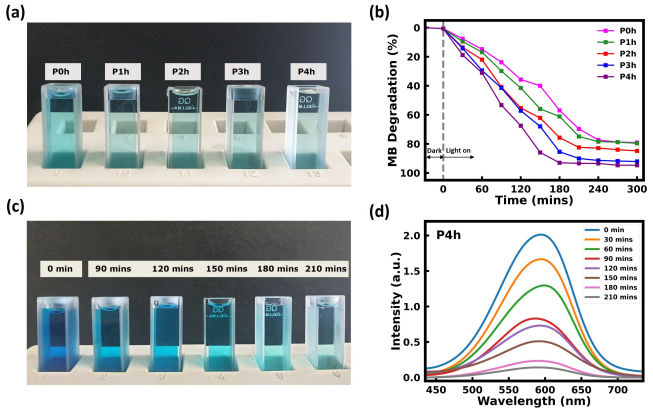

FIGURE 9 (a) The resulting solution after complete MB degradation using all the samples. (b) Photocatalytic degradation of methylene blue using the samples (c) Time-dependent degradation of methylene blue (MB) using the P4h sample for 210 minutes. (d) Spectra from ultraviolet-visible spectroscopy at the absorption peak around 600 nm for MB degradation using the P4h sample.

The x-ray photoelectron spectroscopy data showing the presence of Ti^{3+} states, and the localized gap states obtained from density functional theory calculations, are supported by the photo-degradation of methylene blue under ultraviolet irradiation. It is worth noting that all samples displayed significant degradation of the methylene blue dye over different periods, Figure 9a. The percentage of photo-degradation (D) of the dye is determined based on the initial dye concentration (C_0) and the concentration at the observation time t (C_t) as:

$$D = \left(1 - \frac{C_0}{C_t}\right) \times 100\,\% \tag{3}$$

The optimal point of degradation for methylene blue was determined by its convergence to a specific value. In the case of samples P0h and P1h, this convergence occurred after 240 minutes, resulting in an approximate 74% degradation of methylene blue, Figure 9b. Conversely, sample P4h achieved convergence after just 180 minutes, with a mere 7% of the dye remaining in the solution, Figure 9c. The close similarity between the UV-Vis spectra obtained at 180 minutes and 210 minutes suggests that the optimal degradation time for the P4h sample is 180 minutes, Figure 9d.

To quantitatively evaluate the photocatalytic activity of the catalysts, the reaction rate constants (k) were determined by first-order approximation of the Langmuir-Hinshelwood kinetic equation given as [46]:

$$-ln\left(\frac{C_0}{C_t}\right) = kKt \approx \kappa t \tag{4}$$

k and K are the degradation rate constant and equilibrium constant for the adsorption of methylene blue by the catalyst respectively. κ is the apparent rate constant [47]. The apparent rate constants of 0.018, 0.018, 0.019, 0.022, and 0.025 min^{-1} were obtained for P0h, P1h, P2h, P3 h, and P4h, respectively. The increased apparent rate results from the shallow trap states in the plasma-treated samples that facilitate the separation of photo-generated electron-hole pairs. This allows more sites to become available for the adsorption of water molecules to produce hydroxyl radicals (•OH), and thus increase the degradation rate.

Based on these results, a proposed photo-degradation mechanism of methylene blue using the plasma-treated samples involves an initial step wherein oxygen vacancies are formed within the titanium dioxide lattice. This leads to the formation of a modified material, denoted as TiO_{2-x}, which signifies the presence of oxygen vacancies:

$$TiO_2 + \text{heat} \rightarrow TiO_{2-x} \quad (5)$$

Furthermore, in the presence of these oxygen vacancies, TiO_{2-x} has a high affinity to adsorb oxygen molecules (O_2) onto its surface [48]:

$$TiO_{2-x} + O_2 \rightarrow TiO_{2-x}(O_2) \quad (6)$$

Under the influence of ultraviolet irradiation ($h\nu$), the adsorbed oxygen molecules on TiO_{2-x} becomes energized to an excited state ($TiO_{2-x}(O_2)^*$):

$$TiO_{2-x} + h\nu \rightarrow TiO_{2-x}(O_2)^* \quad (7)$$

The presence of Ti^{3+} species facilitates the transfer of electrons to the adsorbed oxygen, resulting in the formation of super-oxide radicals (O^-) and the conversion of Ti^{3+} to Ti^{4+}:

$$TiO_{2-x}(O_2)^* + Ti^{3+} \rightarrow TiO_{2-x} + O_2^- + Ti^{4+} \quad (8)$$

Finally, the super-oxide radicals proceed to undergo a reaction with water, yielding hydroxyl radicals ($^{\bullet}OH$). This crucial reaction is notably enhanced in the plasma-treated samples, which exhibit improved hydrophilicity – a prerequisite for hydroxyl radical generation. These hydroxyl radicals then interact with the methylene blue dye, catalyzing its degradation into a range of intermediate products and, ultimately, achieving complete mineralization:

$$O_2^- + H_2O \rightarrow \dot{O}H + \dot{O}H \quad (9)$$

$$\text{methylene blue} + \dot{O}H \rightarrow \text{Degradation Products} \quad (10)$$

Electrochemical impedance spectroscopy was employed to investigate the surface charge transfer resistance of the samples, providing valuable insights into their electrochemical behavior. The semicircular Nyquist plot corresponds to the charge transfer resistance at the electrode interface, Figure 10. To analyze this impedance behavior, an equivalent circuit was utilized. The circuit comprises several components: R_B and R_{CT} represent the bulk resistance of the electrolyte and the charge transfer resistance respectively. W is Warburg impedance and CPE corresponds to the constant phase element, inset in Figure 10. The Nyquist plot clearly illustrates that P4h exhibits the smallest semicircle, indicating the most rapid interfacial charge transfer and efficient separation of photo-generated charges. The calculated charge transfer resistances for P0h, P3 h, and P4h were found to be 19.8 Ω, 17.7 Ω, and 16.9 Ω, respectively. These findings suggest that time-dependent air plasma treatment of titanium dioxide effectively retards the recombination of photo-generated charge carriers and facilitates interfacial charge transfer.

To gain deeper insights into the recombination rate of the composite, the photocurrent responses of the samples were also examined. The initial photocurrent responses of the samples upon toggling the ultraviolet on and off showed sharp anodic spikes, indicating the separation of electron/hole pairs at the catalyst/electrolyte interface, Figure 11. Subsequently, a time-dependent

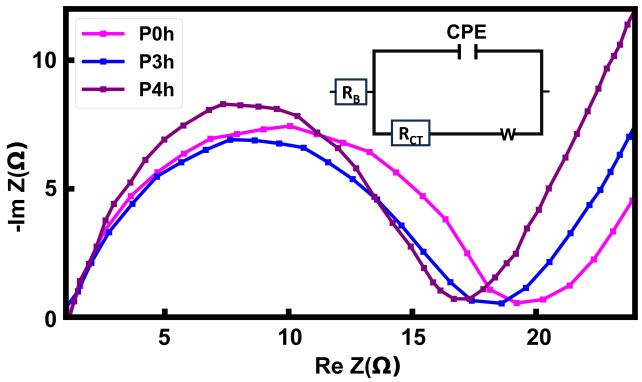

FIGURE 10 Electrochemical impedance spectroscopy Nyquist plots under ultraviolet irradiation. Only the plots for P0h, P3 h, and P4h samples are displayed. The inset depicts the equivalent circuit used for the experiment.

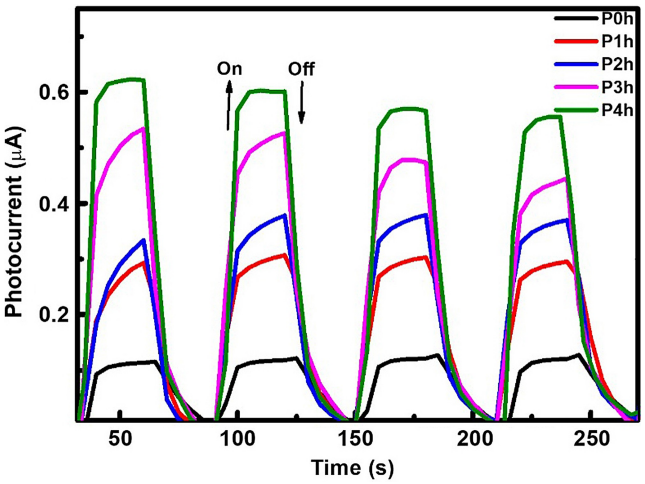

FIGURE 11 Transient photocurrent response under ultraviolet irradiation.

decrease in photocurrent occurs until reaching a steady-state current. This decline signifies the occurrence of electron-hole recombination. At the equilibrium current, a delicate balance is achieved between the competing processes of separation and recombination of electron-hole pairs. Notably, P4h exhibits the highest photocurrent, displaying a pronounced anodic peak. This suggests a delayed recombination process, leading to a more efficient separation of electron/hole pairs. Furthermore, the gradual decay of photocurrent to zero upon light deactivation indicates the release of charge carriers from shallow trap states. This observation implies a higher concentration of oxygen vacancies in P4h resulting from extended plasma treatment.

The reusability of the P4h photocatalyst for methylene blue degradation was examined through the analysis of transient photocurrent response. The P4h photocatalyst was subjected to centrifugation and reused in four consecutive cycles for methylene blue degradation under ultraviolet irradiation. The percentage degradation in cycles 1, 2, 3, and 4 was 93.3%, 91.9%, 90.2%, and 87.8%, respectively. Even after the fourth cycle, the efficiency of the photocatalyst remained above 80%. This demonstrates the excellent stability, sustainability, and reusability of the air plasma-treated titanium dioxide photocatalyst.

4 | CONCLUSIONS

This work highlights a simple and cost-effective modification of titanium dioxide through air plasma treatment as a promising candidate for advanced photocatalytic applications, offering an efficient and sustainable approach to address environmental pollution challenges. Commercial titanium dioxide samples were treated using plasma, under ambient conditions for extended durations, leading to a reduced crystallite size in titanium dioxide. The formation of gap states is also evident, supported by calculations based on density functional theory, which reveals that non-stoichiometric models of titanium dioxide exhibit additional localized states in the gap region between the valence band minimum and conduction band maximum, primarily associated with titanium atoms. Furthermore, the utilization of plasma-treated materials in the degradation of methylene blue demonstrates enhanced performance compared to untreated samples. Particularly noteworthy is the 4-hour plasma-treated photocatalyst, exhibiting commendable stability and reusability.

ACKNOWLEDGEMENTS

C.U. expresses his appreciation to the Nanoscale & Quantum Phenomena Institute (NQPI) for the financial support conferred through the NQPI research fellowship. The authors acknowledge the National Science Foundation (NSF) for computational support through XSEDE (Grant No. ACI-1548562; allocation no. DMR-190008P) and ACCESS (Grant No. 2138259, 2138286, 2138307, 2137603, and 2138296.; allocation no. phy230007p). Basic Science Research Program through the National Research Foundation of Korea (NRF-2020R1I1A3A04037469) also supported this work. The authors thank Anna-Theresa Kirchtag for proofreading the manuscript.

CONFLICT OF INTEREST STATEMENT

The authors declare no financial or commercial conflict of interest.

DATA AVAILABILITY STATEMENT

The data that support the findings of this study are available from the corresponding author upon reasonable request.

ORCID

C. Ugwumadu http://orcid.org/0000-0001-9920-7594
D. A. Drabold http://orcid.org/0000-0001-5344-5837

REFERENCES

1. Z. Mulushewa, W. T. Dinbore, Y. Ayele, *Environ. Anal. Health Toxicol.* **2021**, *36*, e2021007.
2. S. A. Umoren, U. J. Etim, A. U. Israel, *J Mater Env. Sci.* **2013**, *4*, 75.
3. F. Masihi, F. Rezaeitavabe, A. Karimi-Jashni, G. Riefler, *Int. J. Hydrog. Energy.* **2024**, *52*, 295–305.
4. M. Rafique, S. Hajra, M. Irshad, M. Usman, M. Imran, M. A. Assiri, W. M. Ashraf, *ACS Omega.* **2023**, *8*, 25640.
5. F. Parrino, L. Palmisano, *Titanium Dioxide (TiO2) and Its Applications*, Elsevier **2020**.
6. C. Ugwumadu, O. Ibukun, H. K. Jeong, *Chem. Phys. Lett.* **2020**, *757*, 137850.
7. O. Ibukun, P. E. Evans, P. A. Dowben, H. Kyung Jeong, *Chem. Phys.* **2019**, *525*, 110419.
8. J. Schneider, D. Bahnemann, J. Ye, G. L. Puma, D. D. Dionysiou, *Photocatalysis: Fundamentals and Perspectives*, Royal Society Of Chemistry **2016**.
9. A. Hossen, H. M. Solayman, K. H. Leong, L. C. Sim, N. Yaacof, A. Abd Aziz, L. Wu, M. U. Monir, *Results Eng.* **2022**, *16*, 100795.
10. O. Ibukun, H. K. Jeong, *Chem. Phys. Lett.* **2020**, *744*, 137234.
11. O. Ibukun, H. K. Jeong, *Curr. Appl. Phys.* **2020**, *20*, 23.
12. T. S. Rajaraman, S. P. Parikh, V. G. Gandhi, *Chem. Eng. J.* **2020**, *389*, 123918.

13. X. Chen, L. Liu, P. Y. Yu, S. S. Mao, *Science.* **2011**, *331*, 746.
14. M. J. Sampaio, R. R. N. Marques, P. B. Tavares, J. L. Faria, A. M. T. Silva, C. G. Silva, *J. Environ. Chem. Eng.* **2013**, *1*, 945.
15. F. Han, V. S. R. Kambala, M. Srinivasan, D. Rajarathnam, R. Naidu, *Appl. Catal. Gen.* **2009**, *359*, 25.
16. M. Wojtoniszak, B. Zielinska, R. J. Kalenczuk, E. Mijowska, *Mater. Sci. Pol.* **2012**, *30*, 32.
17. A. Sarkar, G. G. Khan, *Nanoscale.* **2019**, *11*, 3414.
18. Q. Wei, Y. Wang, Q. Yang, L. Yu, *J. Ind. Text.* **2007**, *36*, 301.
19. M. J. Shenton, M. C. Lovell-Hoare, G. C. Stevens, *J. Phys. Appl. Phys.* **2001**, *34*, 2754.
20. J.-B. Han, X. Wang, N. Wang, Z.-H. Wei, G.-P. Yu, Z.-G. Zhou, Q.-Q. Wang, *Surf. Coat. Technol.* **2006**, *200*, 4876.
21. Z. Cinar, *Molecules.* **2017**, *22*, 556.
22. Z. Hu, H. Metiu, *J. Phys. Chem. C.* **2011**, *115*, 5841.
23. J. Stausholm-Møller, H. H. Kristoffersen, B. Hinnemann, G. K. H. Madsen, B. Hammer, *J. Chem. Phys.* **2010**, *133*, 144708.
24. N. San, A. Hatipoğlu, G. Koçtürk, Z. Çınar, *J. Photochem. Photobiol. Chem.* **2002**, *146*, 189.
25. W. Navarra, I. Ritacco, O. Sacco, L. Caporaso, M. Farnesi Camellone, V. Venditto, V. Vaiano, *J. Phys. Chem. C.* **2022**, *126*, 7000.
26. B. Prasai, B. Cai, M. K. Underwood, J. P. Lewis, D. A. Drabold, *J. Mater. Sci.* **2012**, *47*, 7515.
27. B. Prasai, B. Cai, D. A. Drabold, M. K. Underwood, J. P. Lewis, in *MS&T-11 Conf. Proc.* **2011**, 12–20.
28. K. Kaur, C. V. Singh, *Energy Procedia.* **2012**, *29*, 291.
29. V. Petkov, G. Holzhüter, U. Tröge, T. Gerber, B. Himmel, *J. Non-Cryst. Solids.* **1998**, *231*, 17.
30. H. J. Kim, C.-S. Yang, H. Jeong, *Chem. Phys. Lett.* **2016**, *644*, 288.
31. T. Niyitanga, H. K. Jeong, *Mater. Chem. Phys.* **2021**, *263*, 124345.
32. G. Ghanashyam, H. K. Jeong, *J. Energy Storage.* **2021**, *40*, 102806.
33. G. Ghanashyam, H. K. Jeong, *Chem. Phys. Lett.* **2022**, *794*, 139492.
34. C. Foo, Y. Li, K. Lebedev, T. Chen, S. Day, C. Tang, S. C. E. Tsang, *Nat. Commun.* **2021**, *12*, 661.
35. J. Khan, L. Han, *in Updates on Titanium. Dioxide*, IntechOpen **2023**.
36. D. A. Drabold, *Eur. Phys. J. B.* **2009**, *68*, 1.
37. J. P. Perdew, K. Burke, M. Ernzerhof, *Phys. Rev. Lett.* **1996**, *77*, 3865.
38. A. Monshi, M. R. Foroughi, M. R. Monshi, *World J. Nano Sci. Eng.* **2012**, *2*, 154.
39. A. Patterso, *J Phys Rev.* **1939**, *56*, 978.
40. L.-Q. Wang, D. R. Baer, M. H. Engelhard, *Surf. Sci.* **1994**, *320*, 295.
41. S.-D. Mo, W. Y. Ching, *Phys. Rev. B.* **1995**, *51*, 13023.
42. T. Zhu, S.-P. Gao, *J. Phys. Chem. C.* **2014**, *118*, 11385.
43. V. Etacheri, C. Di Valentin, J. Schneider, D. Bahnemann, S. C. Pillai, *J. Photochem. Photobiol. C* **2015**, *25*, 1.
44. R. Thapa, C. Ugwumadu, K. Nepal, D. A. Drabold, M. T. M. Shatnawi, *J. Non-Cryst. Solids.* **2023**, *601*, 121998.
45. C. Ugwumadu, K. N. Subedi, R. Thapa, P. Apsangi, S. Swain, M. N. Kozicki, D. A. Drabold, *J. Non-Cryst. Solids* **2023**, *18*, 100179.
46. C. Xu, G. P. Rangaiah, X. S. Zhao, *Ind. Eng. Chem. Res.* **2014**, *53*, 14641.
47. K. V. Kumar, K. Porkodi, F. Rocha, *Catal. Commun.* **2008**, *9*, 82.
48. K. Suriye, P. Praserthdam, B. Jongsomjit, *Appl. Surf. Sci.* **2007**, *253*, 3849.

How to cite this article: C. Ugwumadu, O. Ibukun, H. K. Jeong, D. A. Drabold, *Materialwiss. Werkstofftech.* **2024**, *55*, e202300233. https://doi.org/10.1002/mawe.202300233